Interfacial charge and spin transport in $\mathbb{Z}_2$ topological insulators

Ai Yamakage,[1] Ken-Ichiro Imura,[1,2,3] Jérôme Cayssol,[3,4,5,*] and Yoshio Kuramoto[1]
[1]*Department of Physics, Tohoku University, Sendai 980-8578, Japan*
[2]*Department of Quantum Matter, AdSM, Hiroshima University, Higashi-Hiroshima 739-8530, Japan*
[3]*LOMA (UMR-5798), CNRS and Université Bordeaux 1, F-33045 Talence, France*
[4]*Department of Physics, University of California, Berkeley, California 94720, USA*
[5]*Max-Planck-Institut für Physik Komplexer Systeme, D-01187 Dresden, Germany*
(Received 20 September 2010; published 9 March 2011)

The Kane-Mele model realizes a two-dimensional version of a $\mathbb{Z}_2$ topological insulator as an idealized model of graphene with intrinsic and extrinsic (Rashba) spin-orbit couplings. We study the transport of charge and spin in such a Dirac electron system in the presence of a sharp potential step, that is, a *pn* junction. An electron incident normal to the junction is completely reflected when Rashba coupling is dominant, whereas it is perfectly transmitted when the two types of couplings are balanced. The latter manifests in charge transport as a peak of conductance and a dip in Fano factor. Charge transport occurs in the direction normal to the barrier, whereas a spin current is induced along the barrier that is also localized in its vicinity. It is demonstrated that contributions from interband matrix elements and evanescent modes are responsible for such an interfacial spin Hall current. Our analysis of spin transport is based on the observation that in the case of vanishing Rashba coupling, each channel carries a conserved spin current, whereas only the integrated spin current is a conserved quantity in the general case. The perfect transmission/reflection of charge and conserved spin current is a consequence of reflection symmetry. Finally, we provide a quasiclassical picture of charge and spin transport by imaging flow lines over the entire sample and Veselago lensing (negative refraction).

DOI: 10.1103/PhysRevB.83.125401 PACS number(s): 73.23.−b

I. INTRODUCTION

The role of spin-orbit coupling has been fundamentally reconsidered during the last decade, providing a host of novel effects[1–4] and phases[5–12] with potential applications in spintronics. First, it was predicted that spin-orbit coupling may generate a transverse spin current in response to an applied electric field in both hole- and electron-doped semiconductors.[1,2] These theoretical predictions were promptly followed by an experimental observation of related spin accumulation at the boundary of GaAs samples.[3,4] More recently, the importance of spin-orbit coupling was highlighted even more clearly in the context of a $\mathbb{Z}_2$ topological insulator, in which band inversion due to spin-orbit coupling leads to the appearance of a peculiar, topologically protected, *metallic* surface state.[5–14] In two spatial dimensions, these metallic surface states, which are characteristic of a $\mathbb{Z}_2$ nontrivial state, can be regarded as a time-reversal invariant, that is, a *helical* version of the *chiral* edge states of integer quantum Hall states.

The Kane-Mele model for graphene is a prototype of such a $\mathbb{Z}_2$ topological insulator and describes noninteracting electrons on a honeycomb lattice with both intrinsic and extrinsic spin-orbit couplings.[5,6] In this model the intrinsic spin-orbit coupling conserves the z component of the real spin (s_z) and generates a topological mass term. In contrast, the extrinsic Rashba-type spin-orbit coupling breaks s_z conservation by mixing $s_z = +1/2$ (spin $\uparrow$) and $s_z = -1/2$ (spin $\downarrow$) spin components. When intrinsic spin-orbit coupling dominates the Rashba one, the bulk excitations are gapped and a pair of gapless states counter-propagates along an edge of the sample. Nevertheless, the weakness of the spin-orbit coupling-induced gap[15–17] makes the realization of a $\mathbb{Z}_2$ nontrivial state extremely difficult in graphene. In contrast, similar helical edge states have been predicted[7] and, soon afterward, reported in transport experiments, performed in HgTe/CdTe quantum wells.[8,13,14]

In a recent paper[18] we have shown that charge transport through a potential step allows for investigating the relative strength of intrinsic and extrinsic spin-orbit couplings in the Kane-Mele model. In the absence of spin-orbit coupling, the transmission through electrostatic potential steps has been extensively studied in graphene both experimentally[19–24] and theoretically[25–27] for the purpose of providing a condensed-matter implementation of the relativistic Klein tunneling. In practice, such potential steps can be induced either by a distant gate[19–24] or by metallic contacts.[28,29] This paper deals with supplementary aspects of the charge transport properties outlined in Ref. 18 and, in addition, spin transport along an electrostatic potential step. As a main result, an interfacial spin Hall effect is predicted, in which a spin current flows in the direction transverse to the applied electric field and is mainly localized in the vicinity of the step. Such a nonuniform spin current distribution distinguishes the interfacial spin Hall effect from the bulk spin Hall effect in homogeneous doped semiconductors,[1–4] graphene,[30] and topological insulators.[31]

The paper is organized as follows. In Sec. II, the charge and spin current operators for the Kane-Mele model are derived in the presence of intrinsic and Rashba spin-orbit coupling. It is shown in Sec. III that quantum averages of these operators consist of direct and cross (interference) terms when computed within a generic scattering state. We discuss charge transport in Sec. IV. As the main prediction of this paper, the spin transport along the interface (transverse to the applied electric field) is described thoroughly in Sec. V and possible experimental detection is also discussed therein. Finally, we provide a

quasiclassical picture of the charge and spin transport by imaging flow lines on the entire sample and Veselago lensing (or negative refraction) at the *pn* junction.

II. FORMALISM: CHARGE AND SPIN CURRENTS

Let us consider the Kane-Mele model[5,6] for graphene and find the appropriate form of charge and spin current operators constructed in the framework of this model. We consider various matrix elements of such charge and spin current operators, that is, quantum averages for propagative and evanescent quasiparticles. Characteristic behaviors of such matrix elements are summarized in Table I for future reference.

A. Kane-Mele model

The low-energy Kane-Mele model[5,6] is defined by the Hamiltonian density $H_{\rm KM} = H_0 + H_\Delta + H_R$ with

$$\begin{aligned} H_0 &= \psi^\dagger (p_x \sigma_x \tau_z + p_y \sigma_y)\psi, \\ H_\Delta &= -\psi^\dagger \Delta \sigma_z \tau_z s_z \psi, \\ H_R &= \psi^\dagger \lambda_R (\sigma_y s_x - \sigma_x \tau_z s_y)\psi. \end{aligned} \tag{1}$$

Here σ_i, τ_i, s_i $(i = x, y, z)$ are the Pauli matrices associated with the lattice isospin (A and B sites of the honeycomb lattice), the valley isospin (K and K' points of the reciprocal space), and the real electronic spin, respectively.

The kinetic Hamiltonian H_0 describes graphene in the absence of any spin-orbit interaction. The intrinsic spin-orbit effect (with coupling constant Δ) is described by H_Δ, which preserves all the symmetries of the problem and further conserves the component s_z of the electronic spin. In contrast, the Rashba contribution H_R (with coupling constant λ_R) explicitely breaks the conservation of s_z.

The full Kane-Mele Hamiltonian $H_{\rm KM}$ acts on eight-spinors. Nevertheless, in this paper we only consider intravalley scattering caused by electrostatic potential steps. Hence we focus on the K valley in the following analysis and simply substitute ($\tau_z = 1$) in Eq. (1). The resulting Hamiltonian $H_{\rm KM}^{(K)}$ consists of a 4×4 matrix acting on a spinor of the form ${}^t[\psi_{A\uparrow}, \psi_{B\uparrow}, \psi_{A\downarrow}, \psi_{B\downarrow}]$, where $\uparrow, \downarrow$ stand for real spin.

In the homogeneous case (in the absence of spacially varying potential), the momentum $\boldsymbol{p} = (p_x, p_y)$ is a good quantum number. The single-valley Hamiltonian $H_{\rm KM}^{(K)}$ is diagonalized by the eigenstates $|\alpha\beta\rangle_p$ as

$$H_{\rm KM}^{(K)} |\alpha\beta\rangle_p = E_{\alpha\beta}(\boldsymbol{p}) |\alpha\beta\rangle_p, \tag{2}$$

where indices $\alpha, \beta = \pm 1$ specify the band. The dispersion relation of the band $\alpha\beta$ reads

$$E_{\alpha\beta}(\boldsymbol{p}) = \alpha \sqrt{\boldsymbol{p}^2 + (\Delta + \beta\lambda_R)^2} + \beta\lambda_R, \tag{3}$$

and the corresponding wave function $\psi_{\alpha\beta p}(\boldsymbol{x}) = \langle \boldsymbol{x} | \alpha\beta \rangle_p$ can be expressed as

$$\psi_{\alpha\beta p}(\boldsymbol{x}) = A_{\alpha\beta}(\boldsymbol{p}) \begin{bmatrix} p_x - i p_y \\ E_{\alpha\beta}(\boldsymbol{p}) + \Delta \\ -i\beta (E_{\alpha\beta}(\boldsymbol{p}) + \Delta) \\ -i\beta (p_x + i p_y) \end{bmatrix} e^{i p \cdot x}, \tag{4}$$

with

$$1/A_{\alpha\beta}(\boldsymbol{p}) = \sqrt{2[\boldsymbol{p}^2 + (E_{\alpha\beta}(\boldsymbol{p}) + \Delta)^2] W L}. \tag{5}$$

These wave functions are normalized to represent a unit probability within a rectangular graphene flake of length L (along the x direction) and width W (along the y direction).

In the presence of a potential step or a sample edge, evanescent states appears. Their spectrum and wave functions are given, respectively, by Eqs. (3), (4), and (5), with typically an imaginary p_x. Note also that $\boldsymbol{p}^2 = p_y^2 - |p_x|^2$. Boundedness of the wave function does not allow evanescent modes to exist in an ideally infinite system. They are, nevertheless, ubiquitous in any heterojunctions (near potential steps) or even at a sample termination. The helical edge states, in contrast, occur only at the boundary between two topologically distinguishable phases, each characterized by opposing Z_2 indices. In the case of the Z_2 topological insulator, the Z_2 index distinguishes trivial (even number of Kramer's pairs) vs. nontrivial (odd number of Kramer pairs) insulating states.

B. Charge and spin current operators

We construct here the charge and spin current operators associated with the single-valley Kane-Mele Hamiltonian $H_{\rm KM}^{(K)}$. We simply write the continuity equations for the charge and the s_z component of the electronic spin. The charge and spin density operators [$\rho_c(\boldsymbol{x})$ and $\rho_{s_z}(\boldsymbol{x})$ respectively can be written as

$$\rho_c(\boldsymbol{x}) = -e \psi^\dagger(\boldsymbol{x}) \psi(\boldsymbol{x}), \tag{6}$$

$$\rho_{s_z}(\boldsymbol{x}) = \frac{\hbar}{2} \psi^\dagger(\boldsymbol{x}) s_z \psi(\boldsymbol{x}), \tag{7}$$

TABLE I. Charge and spin current density carried by propagating and evanescent modes. Contributions are also classified to *direct* and *cross* terms (see Sec. III C). Note that the tangential component of momentum p_y is conserved across the junction and always takes a *real* value. Normal and tangential components of the current density are also defined with respect to the interface.

	Direct				Crossed			
	Charge		Spin		Charge		Spin	
	Normal	Tangential	Normal	Tangential	Normal	Tangential	Normal	Tangential
Propagating	$\propto \Re[p_x]$	$\propto p_y$	0	0	0	$\propto \Re[p_x]$	$\propto \Re[p_x]$	$\propto p_y$
Evanescent	0	$\propto p_y$	0	$\propto \Im[p_x]$	0	$\propto \Im[p_x]$	$\propto \Im[p_x]$	$\propto p_y$

using the four-component field operators $\psi(\boldsymbol{x})$ and $\psi^\dagger(\boldsymbol{x})$. The charge current operator $\boldsymbol{J}_c$ is determined such that it satisfies the continuity equation for charge:

$$\frac{\partial \rho_c}{\partial t} + \mathrm{div}\boldsymbol{J}_c = 0. \tag{8}$$

Using the equation of motion

$$i\frac{\partial \psi}{\partial t} = [-i\boldsymbol{\sigma}\cdot\boldsymbol{\nabla} + \lambda_R(\sigma_y s_x - \sigma_x s_y) - \Delta\sigma_z s_z)]\psi, \tag{9}$$

it is readily verified that the operator defined as

$$\boldsymbol{J}_c \equiv -e\psi^\dagger\boldsymbol{\sigma}\psi$$

satisfies Eq. (8). This expression can be obtained alternatively from the usual definition of the charge current,

$$\boldsymbol{J}_c = -e\frac{\partial H_{\mathrm{KM}}^{(K)}}{\partial \boldsymbol{p}},$$

and by noting that only the momentum-dependent part of $H_{\mathrm{KM}}^{(K)}$ is $H_0 = \psi^\dagger \boldsymbol{p}\cdot\boldsymbol{\sigma}\psi$ ($v_F = 1$).

We repeat the same procedure by introducing the spin current operator for the s_z-spin component as

$$\boldsymbol{J}_{s_z} = \frac{\hbar}{2}\psi^\dagger\boldsymbol{\sigma}s_z\psi. \tag{10}$$

However, in the presence of Rashba spin-orbit coupling, the second term on the right-hand side of Eq. (9) does not commute with s_z, leading to a source term in the continuity equation for spin:

$$\frac{\partial \rho_{s_z}}{\partial t} + \mathrm{div}\boldsymbol{J}_{s_z} = \lambda_R\psi^\dagger(\sigma_x s_x + \sigma_y s_y)\psi. \tag{11}$$

The source term $\lambda_{\mathrm{R}}(\sigma_x s_x + \sigma_y s_y)$ describes the spin torque due to Rashba spin orbit interaction. Violation of the continuity equation leads, in many cases, to the ambiguity in the definition of spin current density, correctly reflecting the fact that spin is not conserved. However, as far as spin transport in our junction problem is concerned, we will see in Sec. V that the spin current density defined as Eq. (10) yields a conserved spin current when integrated over the incident angle ϕ. This spin current satisfies the continuity equation *globally*, that is, in the sense of

$$\int_{-p_F}^{p_F}\frac{dp_y}{2\pi}\left(\frac{\partial\langle\rho_{s_z}\rangle}{\partial t} + \mathrm{div}\langle\boldsymbol{J}_{s_z}\rangle\right) = 0, \tag{12}$$

where $\langle\ldots\rangle$ denotes averaging over the scattering states. The spin current density, (10), becomes *locally* conserved in the absence of Rashba spin-orbit coupling: $\lambda_R = 0$.

C. Charge and spin current carried by an eigenstate $|\alpha\beta\rangle_p$

We now evaluate the quantum average of the charge and s_z-spin currents in the eigenstate $|\alpha\beta\rangle_p$ defined by Eq. (4). When both p_x and p_y are real, this state corresponds to a propagating plane wave and carries the charge current density

$$\begin{aligned}\langle\boldsymbol{J}_c\rangle_{\alpha\beta p} &= -e\psi^\dagger_{\alpha\beta p}(\boldsymbol{x})\boldsymbol{\sigma}\psi_{\alpha\beta p}(\boldsymbol{x})\\ &= -4eA^2_{\alpha\beta}(E_{\alpha\beta}(\boldsymbol{p}) + \Delta)\ \boldsymbol{p},\end{aligned} \tag{13}$$

which is collinear to the momentum $\boldsymbol{p}$. This current consists of equal contributions from the channels $s_z = 1$ and $s_z = -1$. Moreover, these contributions correspond to opposite spin currents leading to a cancellation of spin current for the s_z-spin component. This statement is confirmed by direct calculation of the quantum average of the s_z-spin current $\boldsymbol{J}_{s_z}$,

$$\langle\boldsymbol{J}_{s_z}\rangle_{\alpha\beta p} = \psi^\dagger_{\alpha\beta p}(\boldsymbol{x})\boldsymbol{\sigma}s_z\psi_{\alpha\beta p}(\boldsymbol{x}) = \boldsymbol{0}, \tag{14}$$

in the bulk eigenstate $|\alpha\beta\rangle_p$.

In the presence of a potential step or at a sample edge, evanescent states, described by an imaginary p_x, become possible. If we assume a semi-infinite graphene plane extending over the half-plane ($x > 0$), the charge current carried by such an evanescent wave reads

$$\left\langle J_c^x\right\rangle_{\alpha\beta p} = 0, \tag{15}$$

$$\left\langle J_c^y\right\rangle_{\alpha\beta p} = -4eA^2_{\alpha\beta}(E_{\alpha\beta}(\boldsymbol{p}) + \Delta)\ p_y e^{-2|p_x|x}. \tag{16}$$

The current is localized near the interface and flows along the y axis. Moreover the net charge transport vanishes when the sum over p_y is performed.

Finally, the average of the spin current in an evanescent state,

$$\left\langle J_{s_z}^x\right\rangle_{\alpha\beta p} = 0, \tag{17}$$

$$\left\langle J_{s_z}^y\right\rangle_{\alpha\beta p} = -2A^2_{\alpha\beta}(E_{\alpha\beta}(\boldsymbol{p}) + \Delta)\ |p_x|e^{-2|p_x|x}, \tag{18}$$

shares the characteristics of the charge current except that the spin current will not vanish upon p_y integration (see Sec. V).

III. SCATTERING STATES FOR A POTENTIAL STEP

We consider a potential step in a graphene monolayer as shown in Fig. 1 and construct the corresponding scattering states. We evaluate the quantum averages of the charge and spin current densities in a given scattering state. Owing to the spin-orbit coupling (i.e., multiband character of the Kane-Mele model), the structure of those averages is more complicated than the average currents in a pure eigenstate $|\alpha\beta\rangle_p$. Indeed a single incident electron generates two transmitted electronic waves. Therefore the averaged currents contain direct terms involving only one kind of quasiparticles and cross terms describing coherent interferences between the two transmitted waves.

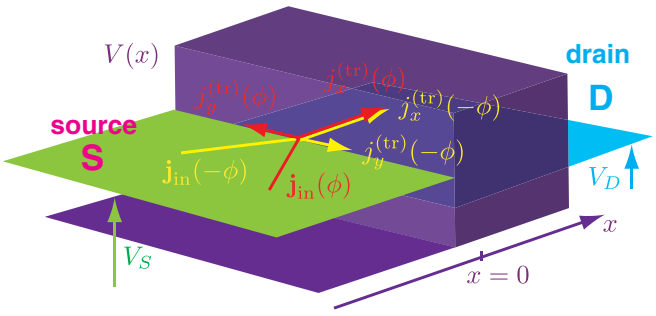

FIG. 1. (Color online) Potential step $V(x)$.

A. The junction model

We consider an electrostatic gate creating a potential step $V(x)$ that is slowly varying on the scale of the atomic lattice. Moreover, we assume an ideally pure system that can be approached in experiments with suspended devices. These conditions ensure that intervalley scattering can be neglected and that the junction is described by the Hamiltonian

$$H = H_{\mathrm{KM}}^{(K)} + \psi^\dagger V(x)\sigma_0 s_0 \psi, \tag{19}$$

where σ_0 and s_0 represent the identity in lattice isospin and real spin space, respectively. Besides, we further assume that the step is sharp on the scale of the Fermi wavelength. In this sense we may represent the potential $V(x)$ by an abrupt step defined by

$$V(x) = \begin{cases} 0 & (x < 0), \\ V_0 & (x > 0). \end{cases} \tag{20}$$

Note that we also assume a straight interface with translational invariance along the y direction (no roughness along the interface $x = 0$).

B. Scattering states

A typical scattering state with energy E and transverse momentum p_y,

$$\Psi_{E,p_y}(\boldsymbol{x}) = \begin{cases} \psi_I(\boldsymbol{x}) + r\psi_R(\boldsymbol{x}) + r_{\mathrm{ev}}\psi_{\mathrm{ev}}(\boldsymbol{x}) & (x < 0) \\ t_+\psi_+(\boldsymbol{x}) + t_-\psi_-(\boldsymbol{x}) \equiv \psi_T(\boldsymbol{x}) & (x > 0) \end{cases}, \tag{21}$$

can be constructed in terms of the bulk eigenstates Eq. (4). It is assumed here that the incident electron is a pure $|+-\rangle_p$ state. Hence the incident and reflected waves read

$$\psi_{I,R}(\boldsymbol{x}) = A(E,\boldsymbol{p}) \begin{bmatrix} \pm p_x - ip_y \\ E + \Delta \\ i(E + \Delta) \\ i(\pm p_x + ip_y) \end{bmatrix} e^{i(\pm p_x x + p_y y)},$$

where $p_x(-p_x)$ corresponds to the incident ψ_I(reflected ψ_R) wave, and

$$1/A(\boldsymbol{p}) = \sqrt{2[\boldsymbol{p}^2 + (E + \Delta)^2]WL}.$$

The x component of the momentum $p_x = p_x(E, p_y)$ is the positive solution of $E_{+-}(p_x, p_y) = E$. There is also an evanescent state defined in the half-plane $x < 0$,

$$\psi_{\mathrm{ev}}(\boldsymbol{x}) = A(E,\boldsymbol{p}) \begin{bmatrix} -i\kappa - ip_y \\ E + \Delta \\ i(E + \Delta) \\ i(-i\kappa + ip_y) \end{bmatrix} e^{\kappa x + ip_y y},$$

and localized near the interface $x = 0$. The value of $\kappa = \kappa(E, p_y)$ is set by the positive solution of $E_{+-}(i\kappa, p_y) = E$.

Within the half-plane $x > 0$, the scattering state consists of two transmitted waves with opposite symmetry $\beta = +$ and $\beta = -$, described by the spinors

$$\psi_\beta(\boldsymbol{x}) = A(E,\boldsymbol{p}) \begin{bmatrix} p_{\beta x} - ip_y \\ E + \Delta \\ -i\beta(E + \Delta) \\ -i\beta(p_{\beta x} + ip_y) \end{bmatrix} e^{i(p_{\beta x} x + p_y y)},$$

where the x components of the momentum $p_{\beta x} = p_{\beta x}(E, p_y)$ are obtained by solving $E_{\alpha\beta}(p_{\beta x}, p_y) = E - V_0$. Note that $p_{\beta x}$ can be either real or imaginary. When $p_{\beta x}$ is real, ψ_β stands for a propagating mode and the sign of p_x is chosen such that the group velocity is positive, that is, correctly describes an outgoing wave. When $p_{\beta x}$ is imaginary, ψ_β is an evanescent mode and the sign of the imaginary part of $p_{\beta x}$ is fixed by the requirement of wave-function boundness at $x \to \infty$.

It is sometimes more convenient to specify $\Psi_{E,p_y}(\boldsymbol{x})$ by E and an incident angle ϕ, instead of E and the transverse momentum p_y:

$$p_x = |\boldsymbol{p}| \cos\phi, \qquad p_y = |\boldsymbol{p}| \sin\phi. \tag{22}$$

Finally, the four scattering amplitudes r, r_{ev}, t_+ and t_- are uniquely determined by solving the continuity condition at $x = 0$:[18]

$$\Psi_{E,p_y}(x = 0^-, y) = \Psi_{E,p_y}(x = 0^+, y) \tag{23}$$

for given E, V_0, and p_y(or ϕ).

C. Direct and cross terms

We have seen that the scattering state $\Psi_{E,p_y}(\boldsymbol{x})$ takes the form of a superposition of two bulk states with opposite band symmetry β. The expectation value of current density in such a scattering state,

$$\begin{aligned} \boldsymbol{J}_{\mathrm{c}} &= -e\psi_T^\dagger \boldsymbol{\sigma} \psi_T \\ &= -e(|t_+|^2 \psi_+^\dagger \boldsymbol{\sigma} \psi_+ + |t_-|^2 \psi_-^\dagger \boldsymbol{\sigma} \psi_- \\ &\quad + 2\Re[t_+^* t_- \psi_+^\dagger \boldsymbol{\sigma} \psi_-]), \end{aligned} \tag{24}$$

has two types of contributions: direct and cross terms. The direct terms (proportional to $|t_+|^2$ and $|t_-|^2$) are similar to those addressed in the previous section; see Eqs. (13)–(18). In particular, such direct terms were shown to carry no net s_z-spin current when associated with a propagative wave [Eq. (14)], whereas evanescent waves carry a finite spin current [Eq. (17)]. In contrast, the cross terms $2\Re[t_+^* t_- \psi_+^\dagger \boldsymbol{\sigma} \psi_-]$ always contribute to spin transport regardless of the nature of the two interfering transmitted waves.

In the following we focus on the charge and spin transport associated with the latter cross terms that mix the transmitted waves ψ_+ and ψ_- altogether. The cross charge current is proportional to the expression

$$\begin{aligned} &-i\psi_+^\dagger \boldsymbol{\sigma} \psi_- \\ &\quad = 2\tilde{A}_+ \tilde{A}_- (\tilde{E} + \Delta) \begin{bmatrix} 0 \\ p_{-x} - p_{+x}^* \end{bmatrix} e^{i(p_{-x} - p_{+x}^*)x}, \end{aligned} \tag{25}$$

where $\tilde{E} = E - V_0$, while p_{+x} and p_{-x} were defined in the previous subsection. These cross terms yield a charge current

along the y axis. In contrast to the direct terms, the cross current has a spacial dependence on the coordinate x (dependence on y is forbidden by translational invariance). The total current is therefore divergenceless.

We now consider the spin current. The cross terms are proportional to

$$\psi_+^\dagger \boldsymbol{\sigma} s_z \psi_- = 2\tilde{A}_+\tilde{A}_-(\tilde{E}+\Delta)\begin{bmatrix} p_{-x}+p_{+x}^* \\ 2p_y \end{bmatrix} e^{i(p_{-x}-p_{+x}^*)x}. \quad (26)$$

The spatial distribution of the spin current is oscillatory if both transmitted states (ψ_+ and ψ_-) are propagative. If one of the transmitted states is propagative while the other is evanescent, the spin current distribution shows damped oscillations. The nature of the currents is summarized in Table I.

The x component of Eq. (26) is generally finite and has an x dependence. The y component of Eq. (26) is also finite but does not contribute to the divergence of the spin current density. Therefore,

$$\mathrm{div}\boldsymbol{J}_{s_z} = \frac{\partial J_{s_z}^x}{\partial x} \neq 0 \quad (27)$$

remains finite due to the cross term. Recall that a spin current density is generally not a conserved quantity; see Eq. (11). In contrast, the contribution from direct terms to the spin current is *divergenceless*. A similar circumstance also occurs in a more conventional semiconductor-based spin Hall system.[32]

IV. CHARGE TRANSPORT

We consider the charge transport across an electrostatic potential step, in the presence of spin-orbit coupling. The charge conductance is directly determined by the transmission probability, whose energy dependences are investigated thoroughly in this section.

A. Pseudoreflection symmetry

The continuum limit of the Kane-Mele model, defined as in Eq. (1), has a pseudoreflection symmetry (PRS) operating in each valley. The PRS with respect to the x axis: $y \to -y$ is expressed as $U = \sigma_x s_y \mathcal{P}$, where $\mathcal{P}$ represents a parity operator in two spatial dimensions, defined by, $\boldsymbol{p} \to \boldsymbol{p}' = \mathcal{P}\boldsymbol{p}\mathcal{P}^{-1} = (p_x, -p_y)$. The spinor part of the eigenstate of the Kane-Mele Hamiltonian, Eq. (1), is also an eigenstate of the PRS operator U, since $[H,U] = 0$, with an eigenvalue, $-\beta$, that is,

$$U\psi_{\alpha\beta p}(\boldsymbol{x}) = -\beta\psi_{\alpha\beta p}(\boldsymbol{x}'). \quad (28)$$

This can be checked explicitly using Eq. (4). We demonstrate that PRS is a convenient tool for clarifying the dependence of reflection and transmission coefficients on incident angles.

B. Transmission at normal incidence

The continuity equation at $x = 0$ reads

$$\psi_I + r\psi_R + r_{\mathrm{ev}}\psi_{\mathrm{ev}} = t_+\psi_+ + t_-\psi_-, \quad (29)$$

where the y component of the momentum is $+p_y$, determining the incident angle ϕ for a given p_x. Applying an operator $\sigma_x s_y$ from the left to the above equation, one finds

$$\psi_I' + r\psi_R' - r_{\mathrm{ev}}\psi_{\mathrm{ev}}' = -t_+\psi_+' + t_-\psi_-'. \quad (30)$$

This can be regarded as the continuity equation for momentum $-p_y$, where $\psi' = \psi|_{p_y=-p_y}$. Comparing the two equations, Eqs. (29) and (30), one can convince oneself that the reflection and transmission coefficients are either an even or an odd function of the incident angle:

$$r' = r, \quad r_{\mathrm{ev}}' = -r_{\mathrm{ev}}, \quad t_+' = -t_+, \quad t_-' = t_-. \quad (31)$$

At normal incidence, $p_y = 0$, two states with an opposing PRS eigenvalue, $-\beta$, are orthogonal to each other at the *spinor level*, that is,

$$\psi^\dagger_{\alpha\beta(p_x,0)}(\mathbf{0})\psi_{\alpha'\beta'(p_x',0)}(\mathbf{0}) \propto \delta_{\beta\beta'} \quad (32)$$

for arbitrary p_x and p_x'. Consequently, the continuity condition, Eq. (23), is decoupled to two equations,

$$r_{\mathrm{ev}}\psi_{\mathrm{ev}} = t_+\psi_+, \quad (33)$$

$$\psi_I + r\psi_R = t_-\psi_-, \quad (34)$$

as far as $p_y = 0$ at the interface $x = 0$. The reflection coefficient r is determined only by the transmitted state with $\beta = -$, therefore the normal incident charge transport is independent of states of symmetry different from that of the incident state. Namely, the transition from $\beta = -$ to $\beta = +$ is impossible due to different symmetry.

Solving Eqs. (33) and (34) yields the reflection coefficient

$$r = \frac{X - Y}{X + Y}, \quad (35)$$

where $X = p_F(E - V_0 + \Delta)$, with p_F being the Fermi momentum on the incident side, $Y = p_{-x}(E + \Delta)$. The reflection probability is given by $R = 1 - |r|^2$.[18] The imaginary p_{-x} that corresponds to the evanescent state $|--\rangle$ leads to perfect reflection $R = 1$ even if the other transmitted state $|-+\rangle$ is propagating. This perfect reflection occurs provided that $\Delta - 2\lambda_R < E - V_0 < -\Delta$ in the dominant Rashba case ($\lambda_R > \Delta$). By contrast, the perfect transmission $r = 0$ occurs at the phase boundary $\lambda_R = \Delta$. Therefore the crossover from perfect reflection to perfect transmission occurs with tuning Rashba spin-orbit coupling.

The upper panel in Fig. 2 shows the normal incident transmission probability T as a function of V_0 and E. The (black) diagonal strip is the region of perfect reflection, which occurs due to the dominant Rashba effect. Upon fixing V_0, E and decreasing λ_R/Δ, the reflection probability decreases as shown in the lower panel in Fig. 2. In the figure all the lines go through the point $\lambda_R/\Delta = 1, T|_{\phi=0} = 1$, namely, perfect transmission *always* occurs, because the Dirac cone appears again at the balanced Rashba and intrinsic spin-orbit case ($\lambda_R/\Delta = 1$). Upon further decreasing λ_R/Δ, the transmission probability decreases and reaches 0 at $\lambda_R/\Delta = (1 - E/\Delta)/2 = 0.25$. Crossover from perfect reflection to perfect transmission occurs due to the competition between Rashba and intrinsic spin orbit in the normal incident case.

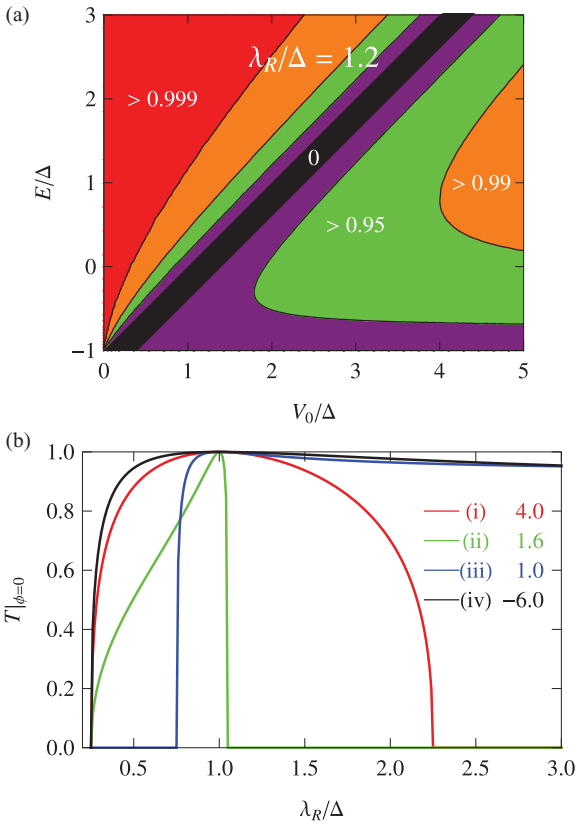

FIG. 2. (Color online) Top: Transmission probability $T(p_y = 0)$ at the normal incidence as a function of V_0/Δ and E/Δ at $\lambda_R/\Delta = 1.2$. Bottom: Dependence of $T(p_y = 0)$ on λ_R/Δ for a fixed value of $(E/\Delta, V_0/\Delta) = (0.5, 2)$. In the upper panel, each region corresponds to a finite range of $T(p_y = 0)$ indicated. In the lower panel, each curve corresponds to different values of V_0/Δ.

C. Charge conductance

Let us consider the rectangular geometry (Fig. 1) with infinite aspect ratio W/L, W and L being the width and length, respectively. We have so far considered the charge current carried by a single scattering channel with definite p_y. In the absence of disorder, the channels are independent and the charge conductance G_c (in units of e^2/h) is simply the sum of the single-channel transmissions $T(p_y)$ over all possible transverse momenta p_y or, equivalently, over all incidence angles:

$$G_c = \frac{e^2}{h}\int_{-Wp_F}^{Wp_F} \frac{d(Wp_y)}{2\pi} T(p_y). \tag{36}$$

We evaluate Eq. (36) explicitly by substituting $T(p_y) = 1 - |r(p_y)|^2$, where the reflection amplitude $r(p_y)$ follows from the continuity condition, Eq. (23). Note that $T \neq |t_+|^2 + |t_-|^2$ because of the potential difference V_0 between the incident and the transmitted side. The obtained charge conductance is shown in Fig. 3 as a function of V_0 for different values of λ_R/Δ. The curves exhibit specific features depending on the value of λ_R/Δ. We leave further inspection of such behaviors to Sec. III C.

Figure 3 shows several conductance curves as a function of V_0/Δ for different values of λ_R. The incident energy is set to be

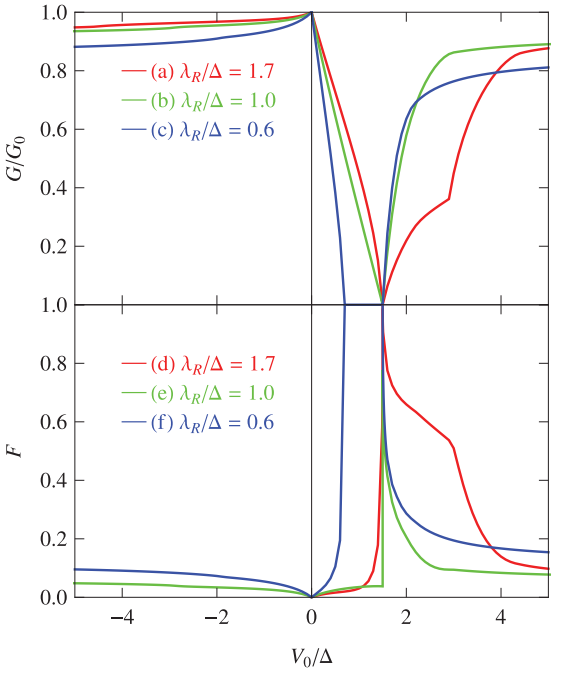

FIG. 3. (Color online) Top: Charge conductance G_c of the potential step (height V_0) normalized by $G_0 = Wp_F/\pi$ ($E/\Delta = 0.5$). Bottom: Fano factor F. Red, blue, and green curves represent the typical behavior of charge conductance in the semimetallic phase ($\lambda_R/\Delta = 1.7$), in the topological gap phase ($\lambda_R/\Delta = 0.6$), and at the phase boundary ($\lambda_R/\Delta = 1$), respectively.

$E/\Delta = 0.5$. The conductance is normalized by $G_0 = Wp_F/\pi$, where p_F is the Fermi wave vector in the incident side.

1. *Semimetalic phase* ($\lambda_R > \Delta$)

When $\lambda_R = 1.7$ [Fig. 3(a), red curve], the system is in the semimetallic phase. The charge neutrality (particle-hole symmetric) point on the transmitted side is located at $V_0/\Delta = E/\Delta + 1 = 1.5$. The conductance *vanishes* at this point. Above this value of V_0, the conductance shows a singularity at $V_0/\Delta = E/\Delta - 1 + 2\lambda_R/\Delta = 2.9$ (discontinuity in the first derivative). Here, the Fermi energy touches the lowest energy band: $|--\rangle$ on the transmitted side. Above this value, the number of energy bands contributing to the conductance is doubled. The conductance shows an abrupt increase in slope (a kink) at this point (see also the Appendix).

Below the neutrality point ($V_0/\Delta = 1.5$), the conductance shows a peak at $V_0 = 0$, then turns to a slow and monotonic decrease as V_0 is decreased. This feature does not seem to resemble its behavior above the neutrality point. Decreasing V_0 from $V_0 = 0$, the Fermi energy touches the highest energy band: $|++\rangle$ at $V_0/\Delta = E/\Delta - 1 - 2\lambda_R/\Delta = -3.9$. But the conductance curve does not show any singularity here.

This asymmetric behavior is a fingerprint of the unique band structure of theKane-Mele model. At $V_0/\Delta = 2.9$, the $|--\rangle$ band touching the Fermi energy has the same band index $\beta = -1$ and, consequently, the same symmetry as the incident state: $|+-\rangle$. Therefore, as soon as this state becomes available for transport, transmission occurs, typically, *at the normal incidence*, leading to an abrupt increase in the conductance. In contrast, at $V_0/\Delta = -3.9$, the $|++\rangle$ band touching the Fermi

surface has a symmetry opposite that of the incident state. Therefore, no transmission occurs at the normal incidence via the $|++\rangle$ band, and the conductance curve bears only a gradual change (see also the Appendix).

Note also that perfect reflection in the semimetallic phase is limited to normal incidence, and the conductance generally takes a finite value due to the contribution from the nonzero incident angle, $\phi \neq 0$, to the right-hand side of Eq. (36). In the case of bilayer graphene, the conductance curve shows similar features, with two shoulders only on the $V_0 > 0$ side.

2. *Topological gap phase* ($\lambda_R < \Delta$)

When $\lambda_R = 0.6$ [Fig. 3(c), blue curve], the system bears a band gap. Naturally, the conductance vanishes identically in the gap region: $-\Delta < E - V_0 < \Delta - 2\lambda_R$, that is, $0.7 < V_0/\Delta < 1.5$. The $|--\rangle$ band is always *activated* for transport in the *pn* regime, $V_0/\Delta > E/\Delta + 1 = 1.5$, showing no singular behavior in the conductance curve.

3. *At the phase boundary* ($\lambda_R = \Delta$)

At the phase boundary [Fig. 3(b), green curve], two bands with $\beta = -$ are combined, and a pair of linearly dispersing energy bands, that is, a Dirac cone, appears. The conductance curve is similar to that of monolayer graphene without spin-orbit interaction.[27] The conductance vanishes at the charge-neutrality point $V_0 = 1.5$ and, again, shows no singularity on the *pn* side.

D. Fano factor

The Fano factor F associated with the potential step is obtained[27] from the transmission probability T as

$$F = \int_{-p_F}^{p_F} dp_y T(1-T) \Big/ \int_{-p_F}^{p_F} dp_y T. \tag{37}$$

The lower panel in Fig. 3 shows the Fano factor as a function of V_0 for different values of λ_R. One of the specific features is that the Fano factor shows, independently of the value of λ_R, a peak structure at $V_0 = E + \Delta = 1.5$, with a maximal value of F (= 1). This is, of course, partly related to the fact that the conductance vanishes at this point. However, recall also that in monolayer graphene without spin-orbit interaction, the Fano factor remains structureless at the corresponding point $V_0 = E$,[27] with a value of $F \approx 0.1$. Such characteristic suppression of shot noise is spoiled by the spin-orbit effects, even when $\lambda_R = \Delta$, where the Dirac cone reappears. A zero conductance leads, trivially, to a peak in the Fano factor. In sharp contrast, the charge conductance is not qualitatively affected by the spin-orbit effects.

The Rashba dominant regime exhibits some anomalous features: a cusp in the conductance at $V_0/\Delta = 2.9$ for $\lambda_R/\Delta = 1.7$ [Fig. 3(d)] and an enhancement of the Fano factor in the regime of perfect reflection. This corresponds to $1.5 < V_0/\Delta < 2.9$ for $\lambda_R/\Delta = 1.7$. In the region of perfect reflection, evanescent modes are dominant in transport at a finite incident angle. The Fano factor is enhanced by such evanescent modes. The Fano factor increases with the increase of Rashba spin-orbit coupling in this regime of perfect reflection. In the balanced case, $\lambda_R = \Delta$ [Fig. 3(e)],

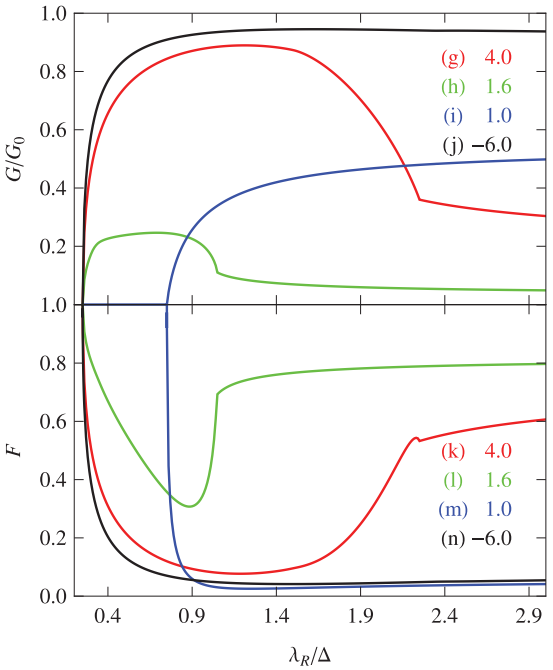

FIG. 4. (Color online) Charge conductance (top) vs. Fano factor (bottom) as a function of Rashba spin-orbit coupling. Incident energy is set to be $E/\Delta = 0.5$. Each curve corresponds to different values of V_0/Δ.

the conductance curves do not differ significantly from the case of no spin-orbit effects ($\lambda_R = \Delta = 0$). In contrast, when intrinsic spin-orbit coupling dominates the Rashba term, that is, in Fig. 3(f), the conductance vanishes within a finite range of V_0, corresponding to the gap. The Fano factor is not well defined and, therefore, is not plotted in this regime of V_0.

In a high and low enough potential region $|V_0/\Delta| \gg 1$ and for arbitrary λ_R, the Fano factor takes a value $F \approx 0.1$, which is roughly the same as the Fano factor without spin-orbit effects, since the transmitted state is free of evanescent modes in this region.

E. Crossover effects in conductance and the Fano factor

The charge conductance and the Fano factor are shown in Fig. 4 as a function of Rashba spin-orbit coupling λ_R/Δ. At a normal incidence, we have seen a crossover from perfect reflection to perfect transmission in the *pn* regime: $V_0/\Delta > 1.5$ (curves i and ii in the lower panel in Fig. 2). As for transport properties, perfect transmission at normal incidence is replaced by a broad maximum near $\lambda_R = \Delta$ [see cases g and h in the upper panel of Fig. 4). The maximum always appears in the *pn* regime. However, unlike the normal incident case, the maximum of charge conductance is not unity and is not precisely located at $\lambda_R = \Delta$ as a consequence of angular integration.

The charge conductance becomes smaller with a decrease in V_0 on the *pn* side (e.g., cases g and h in the upper panel in Fig. 4) and actually vanishes at $V_0/\Delta = 1.5$ (not plotted). This is because the number of propagating states on the transmitted side decreases with the decrease in V_0 (and vanishes at $V_0/\Delta = 1.5$). A cusp of conductance also appears in this regime at the band edge of $|--\rangle$. When λ_R/Δ is larger than this value, the

Fermi energy intersects with only $\beta = +$ band. As a result, perfect reflection occurs at the normal incidence, leading to smaller values of conductance.

In contrast, in the *nn* regime, $V_0/\Delta < 1.5$ (e.g., cases i and j in the upper panel in Fig. 4), a maximum does not appear, because perfect reflection does not occur at the normal incidence (see iii and iv in the lower panel in Fig. 2). When $V_0/\Delta = 1$ (case i), charge conductance vanishes in $\lambda_R/\Delta \leqslant (1 - E/\Delta + V_0/\Delta)/2 = 0.75$, where the system is gapped on the transmitted side.

Dependence of the Fano factor on Rashba spin-orbit coupling is shown in the lower panel in Fig. 4. Interestingly, the lower panel looks almost like the upside-down image of the upper panel.

V. SPIN TRANSPORT

Here we investigate the spin transport generated by an electrostatic potential step in the presence of spin-orbit effects. The potential step splits the graphene sample into two pieces characterized by distinct carrier densities. The spin is drifted along the interface and the spin current is therefore transverse to the applied electric field. This spin Hall effect is a mesoscopic analog of the bulk spin Hall effect occurring in homogeneous electron- or hole-doped semiconductors.[1,2] The present effect requires both spin-orbit coupling and a step in the carrier density. The spin Hall current localized in the vicinity of interface appears also in 2DEG with Rashba spin-orbit interaction.[33]

A. Local spin current density

The spin flows along the y axis, namely, along the interface $x = 0$ defined by the potential step. The total spin current density,

$$j^y_{s_z}(\boldsymbol{x}) = \int_{-p_F}^{p_F} \frac{dp_y}{2\pi} W J^y_{s_z}(\boldsymbol{x}) = \frac{\hbar W}{2} \int_{-p_F}^{p_F} \frac{dp_y}{2\pi} \Psi^\dagger(\boldsymbol{x}) \sigma_y s_z \Psi(\boldsymbol{x}), \tag{38}$$

results from the summation of the single-channel currents $J^y_{s_z}(\boldsymbol{x})$ over all possible transverse modes labeled by their momenta p_y. This local current is maximal near the interface and decays when the distance x is increased (Fig. 5). Note that the spacial dependence of the spin current density $j^y_{s_z}(\boldsymbol{x})$ is determined by a subtle interplay between the direct and the cross terms. When both transmitted waves are propagative, the (single-channel) cross-spin current oscillates as a function of the distance x from the interface. Of course, these oscillations are damped when integrated over all possible transverse momenta p_y (see Fig. 5) but this decay is a long-range power law rather than an exponential decay.

When one or two transmitted wave(s) is(are) evanescent, even the single-channel current decays exponentially when the distance x from the interface is increased. As a result, the total spin current density decays very abruptly with x (see Fig. 5).

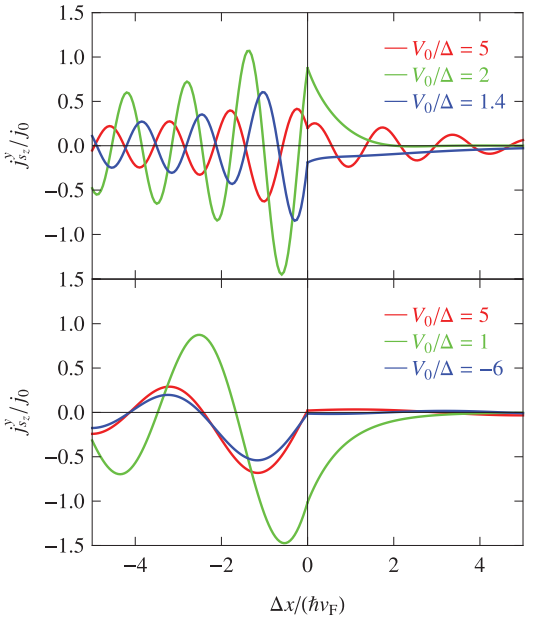

FIG. 5. (Color online) Spatial distribution of spin current density. $\lambda_R/\Delta = 2$ (top) and $\lambda_R/\Delta = 0.5$ (bottom). The spin Hall current is localized in the vicinity of the junction. $j_0 = \Delta/(2\pi L)$.

B. Spin conservation

The same situation occurs for the x component of spin current, which comes only from the cross term, that is, from Eq. (26). Moreover, this contribution, due to spin torque in the presence of Rashba spin-orbit coupling, vanishes after integration over incident angle. The spin transport occurs, therefore, only in the direction parallel to the interface. Besides, the continuity of spin-current density is recovered after this angular averaging. Notice that the spin torque introduced in Eq. (11), that is,

$$\eta \equiv \lambda_R(\sigma_x s_x + \sigma_y s_y), \tag{39}$$

is pseudoreflection odd ($U\eta U^\dagger = -\eta$). The expectation value of this spin torque at a position $\boldsymbol{x}$ on the transmitted side ($x > 0$) is

$$\psi_T^\dagger \eta \psi_T = \sum_{\beta,\beta'=\pm} t^*_\beta t_{\beta'} \psi^\dagger_\beta \eta \psi_{\beta'}. \tag{40}$$

In the case of direct terms, this leads to

$$|t_\beta|^2 \psi^\dagger_\beta \eta \psi_\beta = |t_\beta|^2 \psi^\dagger_\beta U^\dagger U \eta U^\dagger U \psi_\beta = -|t_\beta|^2 \psi^\dagger_\beta \eta \psi_\beta, \tag{41}$$

with the help of Eq. (28). Thus one could see that contributions from direct terms to spin torque vanish, which is consistent with the discussion in Sec. III C. In contrast, the cross terms obey

$$t^*_\beta t_{-\beta} \psi^\dagger_\beta \eta \psi_{-\beta} = -t'^*_\beta t'_{-\beta} \psi'^\dagger_\beta \eta \psi'_{-\beta}, \tag{42}$$

where we have used Eq. (31). Notice also that $\sigma_x s_y \psi_\beta = -\beta \psi'_\beta$. The right-hand side of Eq. (42) is an expectation value of spin torque for an incident momentum $\boldsymbol{p}' = (p_x, -p_y)$.

The cross term is, therefore, an odd function of the incident angle. This quantity, averaged over the incident angle, clearly vanishes. Consequently, the spin torque averaged over the incident angle also vanishes.

The definition of spin current in the Kane-Mele model has been discussed.[34] In general cases, the definition of spin current is not uniquely determined in the presence of Rashba spin-orbit coupling.[35] However, in the junction system we consider here the spin current density, defined as Eq. (10), is thus considered to be a conserved quantity in the sense of Eq. (12) and free of the usual issue of defining a spin current.

C. Results

Figure 5 shows the spatial distribution of spin current density parallel to the interface, that is, the y component of the spin current is plotted as a function of coordinate x normal to the interface for different values of Rashba spin-orbit coupling: $\lambda_R/\Delta = 2$ (dominant Rashba phase) for the upper panel in Fig. 5, and $\lambda_R/\Delta = 0.5$ (topological gap phase) for the lower panel Fig. 5.

In the upper panel, $1.5 < V_0/\Delta < 3.5$ corresponds to the regime of perfect reflection, and the absolute value of spin current is large compared with other cases. The spin current is localized in the vicinity of the interface, explicitly manifesting that spin is carried by evanescent modes (localized in the x direction but propagating in the y direction). It also shows a damped oscillatory behavior for a larger value of V_0, such as $V_0/\Delta = 5$, in the upper panel. Such damped oscillation is an incarnation of cross terms between evanescent and propagating modes. The lower panel in Fig. 5 corresponds to the topological gap phase, in which the spin current takes a large negative value when the Fermi energy is in the gap on the transmitted side.

Figure 6 shows the spin Hall current at $x = 0$. Let us compare it with the charge conductance shown in Fig. 3, both represented as a function of V_0. The two curves indeed show quite contrasting behaviors. At $V_0 = 0$ (in the absence of a junction) the charge conductance shows a maximum (peak). In contrast, the spin current vanishes at $V_0 = 0$, reflecting the fact that, here, spin transport is a mesoscopic effect due to the presence of interface.

Both the magnitude and the sign of the spin current are tuned by V_0. The direction of the spin current is opposite between interband tunneling ($V_0 > E + \Delta$) and intraband tunneling ($V_0 < E + \Delta$) cases (compare the two panels in Fig. 6).[36] The latter also includes the case of the metal-insulator junction. We can confirm this explicitly from Eqs. (18) and (26) with $E \to \tilde{E} = E - V_0$. The direct term of the spin Hall current is proportional to $E - V_0 + \Delta$, therefore the direction changes near $V_0 = E + \Delta$. The sign of the cross term is opposite that of the direct terms and enhanced in the vicinity of the Dirac point $V_0 = E + \Delta$, resulting in a finite spin current at $V_0 = E + \Delta$.

In the dominant Rashba phase ($\lambda_R > \Delta$), two quadratic bands touch at the neutrality point $E = -\Delta$. On the transmitted side, this corresponds to $V_0 = E + \Delta \equiv V_n$. At this value of V_0, the charge conductance vanishes. The spin conductance changes its sign in the vicinity of neutrality point but remains finite precisely on that point (see the lower panel in Fig. 6). This

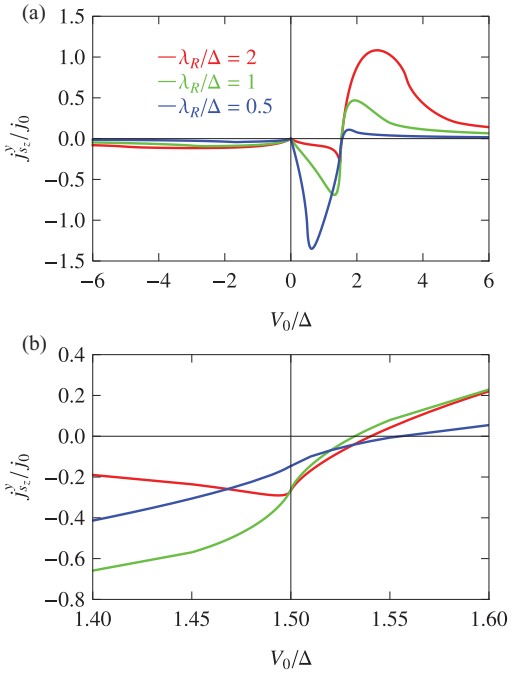

FIG. 6. (Color online) Spin transport in the Kane-Mele p-n junction for different values of λ_R. The p-n junction induces an s_z-spin current in the direction *parallel* to the interface. Such a spin Hall current is plotted at $x = 0$ as a function of V_0.

is again due to the evanescent modes. The spin current takes a large positive value above the neutrality point: $V_0 > V_n$. In the topological gap phase ($\lambda_R < \Delta$), the charge conductances vanishes in the gap, $E - \Delta < V_0 < E + \Delta = V_n$, whereas the spin current is enhanced in the gap, taking a large negative value.

The upper panel in Fig. 7 reveals two different natures of the mesoscopic spin Hall effect by studying, separately, the $\Delta = 0$ and $\lambda_R = 0$ cases. Figure 7 shows that the mesoscopic spin Hall current actually flows in the absence of the topological mass term: $\Delta = 0$. The spin Hall current is enhanced in the regime of perfect reflection: $E < V_0 < E + 2\lambda_R$ ($0.5 < V_0/\lambda_R < 2.5$ in Fig. 7). This corresponds to the regime of V_0 above the neutrality point, where the spin conductance takes a large positive value. The lower panel in Fig. 7 shows, on the contrary, $J^y_{s_z}$ as a function of V_0 in the absence of Rashba spin-orbit coupling: $\lambda_R = 0$. Clearly, the spin current is enhanced when the Fermi energy is in the gap on the transmitted side, $E - \Delta < V_0 < E + \Delta = V_n$ ($0.5 < V_0/\Delta < 2.5$ in Fig. 7), that is, in the situation of the metal-insulator junction. In the region of $V_0 < 0$ and $V_0 > 2E$, the spin current vanishes because only the propagating mode appears. The spin degeneracy remains in the absence of Rashba spin-orbit coupling, and as a result, the cross term also vanishes.

On the transmitted side, the enhancement of the spin Hall current thus occurs for two reasons: (i) perfect reflection in the dominant Rashba phase (on the $V_0 > V_n$ side) and (ii) a topological gap (on the $V_0 < V_n$ side). In the two cases, evanescent modes play a dominant role in the solution of scattering problem at the junction. The enhancement of the spin

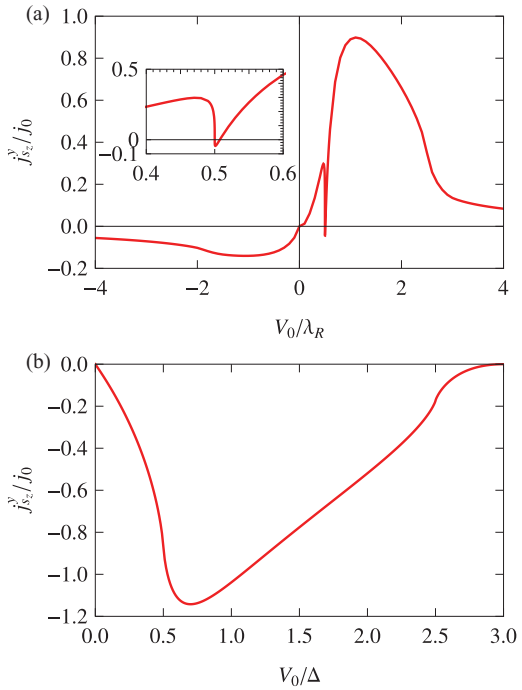

FIG. 7. (Color online) Mesoscopic spin Hall effect in the absence of a topological mass term, $\Delta = 0$ (top), and of Rashba spin-orbit coupling, $\lambda_R = 0$ (bottom). Spin Hall currents at $x = 0$ are plotted as a function of V_0 for $E/\lambda_R = 0.5$ with $\Delta = 0$, $j_0 = \lambda_R/(2\pi L)$, and $E/\Delta = 1.5$ with $\lambda_R = 0$, $j_0 = \Delta/(2\pi L)$.

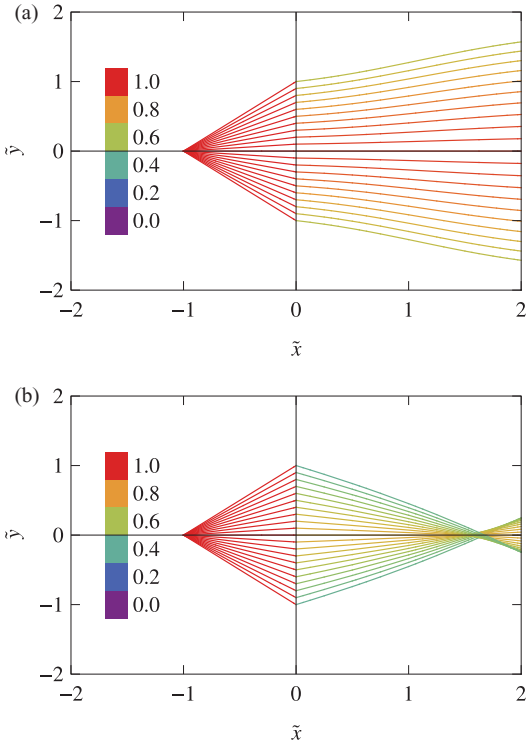

FIG. 8. (Color online) Refraction of electron beams by the potential step in the topological gap phase ($\lambda_R/\Delta = 0.5$). (a) Intraband tunneling ($V_0/\Delta = -2$). (b) Interband tunneling ($V_0/\Delta = 2$). Spatial coordinates: $\tilde{x} = x\Delta/(\hbar v_F)$, $\tilde{y} = y\Delta/(\hbar v_F)$. Fermi energy: $E/\Delta = 0.5$.

Hall current along the interface thus has two different natures, both related to evanescent modes. Depending on which side of the neutrality point the Fermi energy on the transmitted side is, the enhanced spin current flows in the opposite directions.

VI. ELECTRON VESELAGO LENSING

The p-n junction in graphene is expected to serve as an electronic version of the "Veselago lens."[37] The charge current distribution, $\boldsymbol{j}_c(\boldsymbol{x}) = (j^x_c(\boldsymbol{x}), j^y_c(\boldsymbol{x}))$, can be used for imaging the electronic flow around the potential step.[38]

Let us imagine an electronic wave packet emitted from a point $\boldsymbol{x} = (-a,0)$ with $a > 0$. If the wave packet has a center-of-mass momentum $\boldsymbol{p} = (p_x, p_y)$ with $p_y/p_x = \tan\phi$, then the wave packet will be incident at the p-n junction (located at $x = 0$) at $y = a\tan\phi$. Let us consider the trajectory of this wave packet after it goes through the pn junction.

Here, instead of following explicitly the dynamics of such a wave packet, we calculate directly the stationary charge current distribution on the transmitted side, using Eq. (24). Then we consider stream lines of the vector field $\boldsymbol{j}_c(\boldsymbol{x})$. Once $\boldsymbol{j}_c(\boldsymbol{x})$ is known, the differential equation,

$$\frac{dy}{dx} = \frac{j^y_c(\boldsymbol{x})}{j^x_c(\boldsymbol{x})}, \tag{43}$$

determines the locus of a stream line under a given boundary condition, say, $y(x = 0) = a\tan\phi$. Equation (43) determines, in turn, the trajectory of the wave packet emitted from $\boldsymbol{x} = (-a,0)$. As we have seen in Eqs. (13)–(16) and (25), j^y_c has no y dependence, whereas j^x_c has no spatial dependence due to charge conservation. Therefore, with a given boundary condition, Eq. (43) can be trivially integrated to give

$$y(x) = a\tan\phi + \frac{1}{j^x_c}\int_0^x dx'\, j^y_c(x'). \tag{44}$$

Repeating the same procedure for different values of incident angle ϕ, one can draw a set of stream lines visualizing the vector field $\boldsymbol{j}_c(\boldsymbol{x})$. Focusing of such stream lines can be regarded as an electronic version of optical lens. Figures 8 and 9 demonstrate such an electron lens realized at the Kane-Mele p-n junction. A color code specifies the strength of the current flow along each trajectory.

A. Topological gap phase

In the topogical gap phase, the refraction properties are quite similar to the ones studied previously for graphene p–n junctions in the absence of spin-orbit interaction.[37] Indeed the y component of the current density changes its sign on crossing the p-n junction, thereby realizing the negative or Veselago-like electronic refraction. In the presence of spin-orbit coupling, the system no longer show perfect focusing [Fig. 8(b)].

In contrast, for an n-n junction (intraband transmission) the y component of the current has the *same* sign on both sides of the junction, indicating that the refractive index is *positive*. As a result, the outgoing electron beam is divergent [Fig. 8(a)].

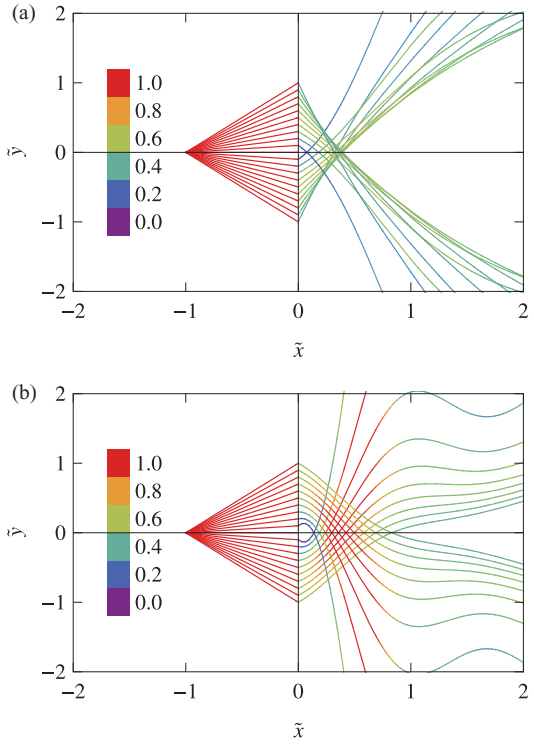

FIG. 9. (Color online) Electron Veselago lens: semimetallic phase ($\lambda_R/\Delta = 2$). Spatial coordinates: $\tilde{x} = x\Delta/(\hbar v_F)$, $\tilde{y} = y\Delta/(\hbar v_F)$. Fermi energy: $E/\Delta = 0.5$. The height of the potential step V_0 is chosen such that (a) $V_0/\Delta = 2$ and (b) $V_0/\Delta = 3.5$, both corresponding to the interband tunneling case. Case (b) corresponds to the opening of the lowest energy channel.

B. Semimetallic phase

More interesting are the refraction properties of the semimetallic phase. Indeed the evanescent modes manifest themselves by the bending of the electronic rays on the transmitted side (Fig. 9). Moreover, no transmission is allowed at the normal incidence, which yields a shade area behind the origin O(0,0) (Fig. 9).

Figure 9 shows a Veselago-like electron lens in the semimetallic phase ($\lambda_R/\Delta = 2$) for two distinct steps V_0: (a) $V_0/\Delta = 2$ (left) and (b) $V_0/\Delta = 3.5$ (right), both corresponding to a *p-n* junction (interband tunneling). In case b, the Fermi energy is touching the top of the $|-,-\rangle$-band, which happens when $V_0 = E - \Delta + 2\lambda_R$. As the Fermi energy approaches the top of the $|-,-\rangle$-band, the *cross* term between propagating (due to $|-,+\rangle$-band) and evanescent (due to $|-,-\rangle$-band) modes plays a significant role. The meandering stream lines in case b are a consequence of such "cross-term transport." It should also be noticed that the shaded area is much more pronounced in case b. Indeed, one can observe that the refractive index becomes positive in the vicinity of the shaded area. Due to perfect reflection at the normal incidence, the x component of the current density is virtually 0 for a small incident angle ϕ. As a result, the electron beam is strongly refracted, with divergent j_y/j_x on the transmitted side (as $\phi \to 0$). This leads to the formation of the shaded area (see Fig. 10 for detailed plots).

Study of electron lens behavior thus reveals rich mesoscopic transport properties of the Kane-Mele *pn* junction. It should

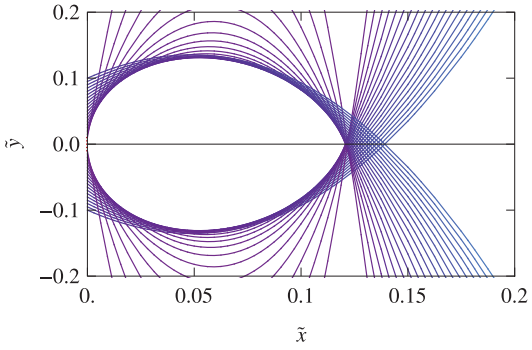

FIG. 10. (Color online) Detailed plots of the shaded region in Fig. 9(b): $\lambda_R/\Delta = 2$, $V_0/\Delta = 3.5$. Other parameters are also the same.

be emphasized that this unique mesoscopic transport is carried out by the evanescent modes and the cross terms. The former enable transport along the edge even when the Fermi level is in the gap on the transmitted side.[39]

Finally, the striking difference between the behavior of the topological gap phase (Fig. 8) and that of the semimetallic phase (Fig. 9) might be observed by scanning probe measurements similar to those successfully implemented on top of ballistic two-dimensional electron gases.[40,41]

VII. CONCLUSION

We have studied theoretically charge and spin transport at a potential step (both *n-n* and *p-n* junctions) within the Kane-Mele of graphene. We have highlighted the role of reflection symmetry associated with the band index β in the crossover from *perfect* reflection to transmission while tuning the Rashba coupling λ_R. We have also computed experimentally measurable quantities such as conductance and the Fano factor.

Due to the multiband character of the model, one incident electron yields two distinct transmitted quasiparticles. The spin Hall current, which is mainly localized in the vicinity of the interface, results from the superposition of two types of contributions: (i) direct terms involving one kind of transmitted quasiparticles and (ii) cross terms describing interferences between the two kinds of transmitted quasiparticles (Sec. V). The direct terms were shown to carry no net s_z-spin current when associated with a propagative wave, whereas evanescent waves carry a finite spin current. In contrast, the cross terms always contribute to spin transport, regardless of the nature of the waves. The interplay between these direct and cross terms is also important for charge transport (Sec. IV). The spin Hall current, which shows a damped oscillation in the vicinity of the interface, induces spin accumulation at the edge with spatial dependence. At low energies, $E \sim V \sim \Delta \sim \lambda_R$, the typical length scale of oscillating and damping is of the order of $\hbar v_F/\Delta$. This value is estimated as $\hbar v_F/\Delta \sim 100\mu$m for $\Delta \sim 1$ K. In real systems the typical length scale may be cut off by the scattering length. We expect that such spin accumulation can, in principle, be detected by an optical measurement.[3]

Moreover, the electronic flow exhibits a large variety of patterns (Sec. VI). In particular, a dominant Rashba spin-orbit coupling (semimetallic phase) leads to curved rays owing to the

presence of evanescent states, whereas rays are still straight for dominant intrinsic spin-orbit coupling (topological gap phase). Note that in a monolayer graphene without spin-orbit coupling, stream lines are straight and refracted only at the interface. In principle, it should be possible to identify those contrasted shapes by scanning a charged tip above the graphene flake as was performed for two-dimensional electron gases in GaAs heterostructures.[40,41] Finally, detecting a clear fingerprint of the role of spin-orbit coupling in transport measurements in graphene seems not impossible but difficult, since the magnitude of spin-orbit coupling is small in graphene, at most, of the order of $\sim$1 K.[42] An alternative way to probe such unique transport characteristics of the *p-n* junction may be to use materials with stronger spin-orbit coupling, such as HgTe/CdTe heterostructures.

ACKNOWLEDGMENTS

A.Y. and K.I. were supported by KAKENHI (K.I., Grant-in-Aid for Young Scientists under Grant No. B-19740189; A.Y., Grant No. 08J56061 from MEXT, Japan). J.C. was supported by the Seventh European Community Framework Programme under Contract TEMSSOC (joint program between University of California, Berkeley, and the Max-Planck-Institut für Physik Komplexer Systeme, Dresden). J.C. acknowledges support from the Agence Nationale de la Recherche under contract 2010-BLANC-041902 (ISOTOP).

APPENDIX: ASYMPTOTIC BEHAVIOR OF CONDUCTANCE

The curve of $\lambda_R/\Delta = 1.7$ in Fig. 3 illustrates the characteristic features of charge conductance in the semimetallic phase: $\lambda_R > 1$. The conductance curve shows, say, at $\lambda_R = 1.7$, a kink structure at $V_0 = E - \Delta + 2\lambda_R = 2.9$, upon opening of the $|--\rangle$ channel to transmission. The purpose of this Appendix is to estimate the asymptotic behavior of G_c in the vicinity of this singularity.

In Sec. IV C we estimated G_c by substituting $T(\phi) = 1 - |r(\phi)|^2$, with $r(\phi)$ determined by continuity condition (23), into the Landauer formula, Eq. (36). Here, to reveal the nature of singularity at $V_0 = E - \Delta + 2\lambda_R$, we extract the contribution of the $|--\rangle$ band to G_c and analyze its asymptotic behavior in the vicinity of the singularity (see Fig. 11). Let us introduce δV, the height of the potential barrier measured from the singularity:

$$\delta V \equiv V_0 - E + \Delta - 2\lambda_R. \tag{A1}$$

When $\delta V \leqslant 0$, the $|--\rangle$ band gives no contribution to the charge current on the transmitted side, since the state is evanescent. When $\delta V > 0$, a propagating mode becomes possible, with the momentum

$$\hbar v_F q_- = -\sqrt{2(\lambda_R - \Delta)\delta V - (\hbar v_F k \sin\phi)^2}, \tag{A2}$$

obtained from the energy conservation, $E_{\alpha\beta}(p_{\beta x}, p_y) = E - V_0$, provided that $|\phi| \leqslant \phi_m$, where the critical angle ϕ_m is defined by

$$(\hbar v_F k \sin\phi_m)^2 = 2(\lambda_R - \Delta)\delta V. \tag{A3}$$

In the limit of $\delta V \to 0$, this reduces to

$$\phi_m \sim \sqrt{2(\lambda_R - \Delta)\delta V}/(\hbar v_F k). \tag{A4}$$

The charge current transmitted to the lowest energy band is given by

$$j_-(\epsilon_F, \phi) = -\frac{e v_F}{WL}\frac{2|t_-|^2 \hbar v_F q_-}{E - V_0 + \lambda_R}, \tag{A5}$$

from Eq. (13). Integrating over all incident angles, one finds

$$\int_{-\phi_m}^{\phi_m} d\phi\, j_-(E,\phi) \sim 2\phi_m\, j_-(\epsilon_F, 0) = \frac{8\delta V}{E + \lambda_R}\sqrt{\frac{E + \Delta}{E - \Delta + 2\lambda_R}}. \tag{A6}$$

The charge current transmitted to the $|--\rangle$ band thus shows a *linear* uprise (proportional to δV) when $\delta V > 0$. As a result, the charge conductance shows an abrupt increase in slope at $V_0 = E + \Delta$. Note that $t_-(E, 0) \neq 0$, thanks to the same symmetry, that is, the same β ($= -1$), for the $|--\rangle$-band as for the incident energy band, $|+-\rangle$.

Similarly, we investigated the asymptotic behavior of G_c in the vicinity of the opening of the $|++\rangle$ channel at $V_0 = E - \Delta - 2\lambda_R$. However, the $|++\rangle$ band (final state) has the opposite symmetry (opposite β) to the initial state: $|+-\rangle$. Due to this mismatch of symmetry, the transmission coefficient $t_+(\phi = 0)$ vanishes even when $V_0 \leqslant E - \Delta - 2\lambda_R$. As a result, the leading-order contribution to the charge conductance starts at second order, that is, $\propto \delta V^2$ (see Fig. 11, right).

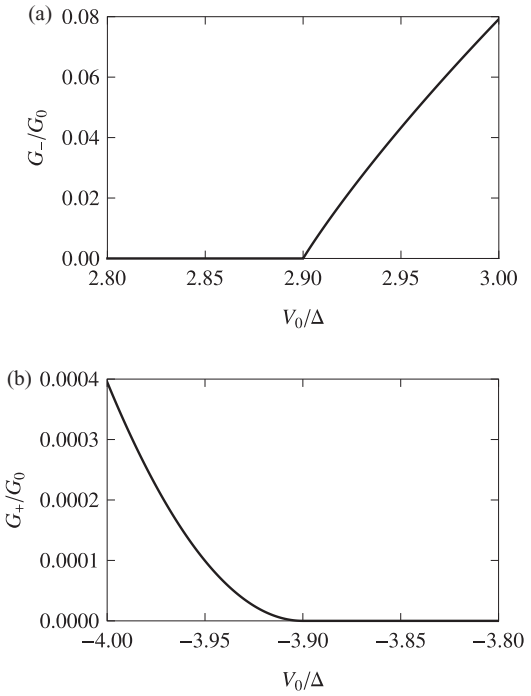

FIG. 11. Contribution of the $|--\rangle$ band to charge conductance. Top: Charge conductance G_- calculated from j_-. Bottom: Charge conductance G_+ calculated from j_+. The system's parameters are chosen such that $\lambda_R/\Delta = 1.7$, $E/\Delta = 0.5$.

*j.cayssol@cpmoh.u-bordeaux1.fr

[1] S. Murakami, N. Nagaosa, and S.-C. Zhang, Science **301**, 1348 (2003).

[2] J. Sinova, D. Culcer, Q. Niu, N. A. Sinitsyn, T. Jungwirth, and A. H. MacDonald, Phys. Rev. Lett. **92**, 126603 (2004).

[3] Y. K. Kato, R. C. Myers, A. C. Gossard, and D. D. Awschalom, Science **306**, 1910 (2004).

[4] J. Wunderlich, B. Kaestner, J. Sinova, and T. Jungwirth, Phys. Rev. Lett. **94**, 047204 (2005).

[5] C. L. Kane and E. J. Mele, Phys. Rev. Lett. **95**, 226801 (2005).

[6] C. L. Kane and E. J. Mele, Phys. Rev. Lett. **95**, 146802 (2005).

[7] B. A. Bernevig, T. L. Hughes, and S.-C. Zhang, Science **314**, 1757 (2006).

[8] M. König, H. Buhmann, L. W. Molenkamp, T. L. Hughes, C. X. Liu, X.-L. Qi, and S.-C. Zhang, J. Phys. Soc. Jpn. **77**, 031007 (2008).

[9] X.-L. Qi and S.-C. Zhang, Phys. Today **63**, 33 (2010).

[10] J. E. Moore, Nature **464**, 194 (2010).

[11] M. Z. Hasan and C. L. Kane, Rev. Mod. Phys. **82**, 3045 (2010).

[12] X.-L. Qi and S.-C. Zhang, e-print arXiv:1008.2026.

[13] M. König, S. Wiedmann, C. Brüne, A. Roth, H. Buhmann, L. W. Molenkamp, X.-L. Qi, and S.-C. Zhang, Science **318**, 766 (2007).

[14] A. Roth, C. Brüne, H. Buhmann, L. W. Molenkamp, J. Maciejko, X.-L. Qi, and S.-C. Zhang, Science **325**, 294 (2009).

[15] H. Min, J. E. Hill, N. A. Sinitsyn, B. R. Sahu, L. Kleinman, and A. H. MacDonald, Phys. Rev. B **74**, 165310 (2006).

[16] D. Huertas-Hernando, F. Guinea, and A. Brataas, Phys. Rev. B **74**, 155426 (2006).

[17] Y. Yao, F. Yei, X. L. Qi, S.-C. Zhang, and Z. Fang, Phys. Rev. B **75**, 041401 (2007).

[18] A. Yamakage, K. I. Imura, J. Cayssol, and Y. Kuramoto, Europhys. Lett. **87**, 47005 (2009).

[19] B. Huard, J. A. Sulpizio, N. Stander, K. Todd, B. Yang, and D. Goldhaber-Gordon, Phys. Rev. Lett. **98**, 236803 (2007).

[20] J. R. Williams, L. DiCarlo, and C. M. Marcus, Science **317**, 638 (2007).

[21] B. Özyilmaz, P. Jarillo-Herrero, D. Efetov, D. A. Abanin, L. S. Levitov, and P. Kim, Phys. Rev. Lett. **99**, 166804 (2007).

[22] J. B. Oostinga, H. B. Heersche, X. Liu, A. F. Morpurgo, and L. M. K. Vandersypen, Nat. Mater. **7**, 151 (2008).

[23] R. V. Gorbachev, A. S. Mayorov, A. K. Saychenko, D. W. Horsell, and F. Guinea, Nano Lett. **8**, 1995 (2008).

[24] G. Liu, J. J. Velasco, W. Bao, and C. N. Lau, Appl. Phys. Lett. **92**, 203103 (2008).

[25] M. I. Katsnelson, K. S. Novoselov, and A. K. Geim, Nature Phys. **2**, 620 (2006).

[26] V. V. Cheianov and V. I. Falko, Phys. Rev. B **74**, 041403 (2006).

[27] J. Cayssol, B. Huard, and D. Goldhaber-Gordon, Phys. Rev. B **79**, 075428 (2009).

[28] B. Huard, N. Stander, J. A. Sulpizio, and D. Goldhaber-Gordon, Phys. Rev. B **78**, 121402 (2008).

[29] N. Stander, B. Huard, and D. Goldhaber-Gordon, Phys. Rev. Lett. **102**, 026807 (2009).

[30] A. Dyrdał, V. K. Dugaev, and J. Barnaś, Phys. Rev. B **80**, 155444 (2009).

[31] Balazs Dora and Roderich Moessner, Phys. Rev. B **83**, 073403 (2011).

[32] S. Murakami, N. Nagaosa, and S.-C. Zhang, Phys. Rev. B **69**, 235206 (2004).

[33] I. Adagideli and G. E. W. Bauer, Phys. Rev. Lett **95**, 256602 (2005).

[34] K. Sengupta, R. Roy, and M. Maiti, Phys. Rev. B **74**, 094505 (2006).

[35] E. B. Sonin, Phys. Rev. B **76**, 033306 (2007).

[36] Some anomalous behaviors can be seen in the vicinity of $V_0 = E + \Delta$, though.

[37] V. V. Cheianov, V. Fal'ko, and B. L. Altshuler, Science **315**, 1252 (2007).

[38] J. Cserti, A. Palyi, and C. Peterfalvi, Phys. Rev. Lett **99**, 246801 (2007).

[39] V. A. Yampol'skii, S. S. Apostolov, Z. A. Maizelis, A. Levchenko, and F. Nori, (2009).

[40] M. Topinka, B. LeRoy, S. Shaw, E. Heller, R. Westervelt, K. Maranowskik, and A. Gossard, Science **289**, 2323 (2000).

[41] M. Topinka, B. LeRoy, R. Westervelt, S. Shaw, R. Fleischmann, E. Heller, K. Maranowskik, and A. Gossard, Nature **410**, 183 (2001).

[42] M. Gmitra, S. Konschuh, C. Ertler, C. Ambrosch-Draxl, and J. Fabian, Phys. Rev. B **80**, 235431 (2009).